

Downward-propagating eruption following vent unloading implies no direct magmatic trigger for the 2018 lateral collapse of Anak Krakatau

Kyra S. Cutler[1,2*], Sebastian F. L. Watt[1], Mike Cassidy[2], Amber L. Madden-Nadeau[2], Samantha L. Engwell[3], Mirzam Abdurrachman[4], Muhammad E. M. Nurshal[4], David R. Tappin[5,9], Steven N. Carey[6], Alessandro Novellino[5], Catherine Hayer[7], James E. Hunt[8], Simon J. Day[9], Stephan T. Grilli[6,10], Idham A. Kurniawan[4] and Nugraha Kartadinata[11]

[1] School of Geography, Earth and Environmental Sciences, University of Birmingham, Edgbaston, Birmingham, B15 2TT, UK

[2] Department of Earth Sciences, University of Oxford, South Parks Road, Oxford OX1 3AN, UK

[3] British Geological Survey, The Lyell Centre, Research Avenue South, Edinburgh EH14 4AP, UK

[4] Faculty of Earth Sciences and Technology, Institut Teknologi Bandung, Jalan Ganesa No. 10 Bandung 40132, West Java, Indonesia

[5] British Geological Survey, Nicker Hill, Keyworth, Nottingham NG12 5GG, UK

[6] Graduate School of Oceanography, University of Rhode Island, Narragansett, R.I 02882, USA

[7] Department of Earth and Environmental Sciences, The University of Manchester, Oxford Road, Manchester M13 9PL, UK

[8] National Oceanography Centre, Waterfront Campus, University of Southampton, European Way, Southampton, SO14 3ZH, UK

[9] Institute for Risk and Disaster Reduction, University College London, London, WC1E 6BT, UK

[10] Department of Ocean Engineering, University of Rhode Island, Narragansett, R.I 02882, USA

[11] Volcano Research and Monitoring Division, CVGHM - Geological Agency of Indonesia, Jl. Diponegoro No. 57, Bandung, 40228, Indonesia

* Corresponding author at: Department of Earth Sciences, University of Oxford, South Parks Road, Oxford OX1 3AN, UK

Email: kyra.cutler@stx.ox.ac.uk

Abstract

The lateral collapse of Anak Krakatau volcano, Indonesia, in December 2018, highlighted the potentially devastating impacts of volcanic edifice instability. The trigger for the Anak Krakatau collapse remains obscure; the volcano had been erupting for the previous six months, and although failure was followed by intense explosive activity, it is the period immediately prior to collapse that is potentially key in providing identifiable, pre-collapse warning signals. Here, we integrate physical, microtextural and geochemical characterisation of tephra deposits spanning the collapse period. We demonstrate that the first post-collapse eruptive phase (erupting juvenile clasts with a low microlite areal number density and relatively large microlites, reflecting crystal growth) is best explained by instantaneous unloading of a relatively stagnant upper conduit. This was followed by the second post-collapse phase, on a timescale of hours, which tapped successively deeper portions of the plumbing system, reflected in highly anorthitic microlite populations, alongside higher calculated ascent velocities and decompression rates, within the post-collapse tephra-stratigraphy. This implies downward propagating destabilisation of the magma storage system, as a response to collapse, rather than pre-collapse magma ascent triggering failure. Importantly, this suggests that the collapse was a consequence of longer-term processes linked to edifice growth and instability, and that no indicative changes in the magmatic system could have signalled the potential for incipient failure. Therefore, monitoring efforts may need to focus on integrating short- and long-term edifice growth and deformation patterns to identify increased susceptibility to lateral collapse. The post-collapse eruptive pattern also suggests a magma pressurisation regime that is highly sensitive to surface-driven perturbations, which led to elevated magma fluxes after collapse and rapid edifice regrowth. Not

only does rapid regrowth potentially obscure evidence of past collapses, but it also emphasises the finely balanced relationship between edifice loading and crustal magma storage.

Keywords: volcanic lateral collapse; sector collapse; magma ascent; microlites; Anak Krakatau; rapid decompression; post-collapse volcanism

Graphical abstract:

1. Introduction

Landslides generated by volcanic flank failure are significant hazards and can cause destructive tsunamis in island settings. Due to their relatively low frequency, very few lateral collapses have been well observed, and there remains limited understanding of the precursors to collapse. Determining the trigger(s) for collapse is often difficult, as edifice instability can develop from a range of factors including gravitational and structural weaknesses, shallow magmatic intrusions and hydrothermal alteration (e.g., Siebert et al., 1987; López and Williams, 1993; McGuire, 2003). However, it is important to constrain the factors driving failure, and particularly whether shifts in magmatic activity are implicated, in order to develop a systematic monitoring framework that could potentially identify signals of incipient collapse.

The lateral collapse of Anak Krakatau, Indonesia, on 22 December 2018, which induced a tsunami causing over 400 fatalities on surrounding coastlines (Grilli et al., 2019), both highlights the impacts of such events and provides an opportunity to better understand the processes that lead to volcanic edifice failure. Anak Krakatau is a small stratovolcano within the Sunda Strait, positioned on the NE edge of the 1883 Krakatau caldera (Deplus et al.,1995). The volcano emerged above sea-level in 1927, developing rapidly through frequent eruptions to a pre-collapse height of 330 m (Grilli et al., 2019). Collapse of its SW flank, with a volume of 0.18-0.31 km^3 (Hunt et al., in press), occurred six months into an eruption phase characterised by Strombolian, Vulcanian and effusive activity. Although this activity was typical of previous decades (e.g., Abdurrachman et al., 2018), it involved a relatively elevated magma flux (Walter et al., 2019). Infrared data from the Moderate Resolution Imaging Spectroradiometer (MODIS) revealed the volcano's highest thermal levels since MODIS measurements began in 2000. However, these were particularly elevated during late September 2018 (Walter et al., 2019), rather than showing a clear temporal progression that culminated in collapse. It thus remains unclear if the collapse was directly initiated by a discrete and identifiable shift in magmatic activity, or if collapse resulted from longer-term growth and destabilisation. What is clear is that the collapse was accompanied (as far as the temporal resolution limits of geophysical observations can constrain) and/or immediately followed by intense explosive activity. The collapse cut the active conduit beneath sea-level, resulting in Surtseyan eruptions that produced extensive ash deposits, rapidly buried the collapse scar, fed convective atmospheric plumes reaching 16-18 km (Prata et al., 2020), and involved a higher magma flux than anything recorded in recent decades (Gouhier and Paris, 2019). Here, we seek to determine the role of magmatic activity in the 2018 Anak Krakatau collapse, specifically addressing whether the intense accompanying volcanism was a driver or a consequence of edifice failure, by reconstructing magma ascent conditions spanning the syn- and post-collapse period. This is important not only to understand this particular event, but more generally to identify causes of edifice failure at both active and inactive volcanoes, to develop approaches for monitoring edifice stability, and to understand the relationship between surface mass redistribution and magma ascent behaviour (cf. Petrone et al., 2009; Watt, 2019).

2. 2018 eruption and collapse observations

Observations in the period spanning the collapse provide important constraints for understanding eruptive behaviour, ash dispersal, and characteristics of the post-collapse tephra-stratigraphy. All times stated in this section are Western Indonesian Time (WIB; UTC + 7 hours).

The 2018 eruption began in late June (PVMBG, 2018). Discharge rates, calculated from MODIS data, indicate that the magma flux peaked in September, gradually waning after October. Intensified eruptions on 22 December produced another peak in activity, but discharge rates had reached comparable or higher levels on ten previous occasions between June and December (Walter et al., 2019). Fishermen, familiar with the area, were located near the island during the collapse, and reported that the activity on 22 December had increased but was not unusual (Perttu et al., 2020). Infrasound signals suggest intense activity started at ~13:00 on 22 December, an interpretation confirmed by eyewitness reports (from the Javan coast) of audible and visible Strombolian eruptions. The infrasound signals were similar in intensity to those from elevated eruption phases in 1999 and October 2018 (Perttu et al., 2020).

Although the June-December 2018 activity was not atypical in style, it is estimated to have added 54 million tons of rock onto Anak Krakatau's central cone and southern flank (Walter et al., 2019). SW deformation of the flank is identifiable from Interferometric Synthetic Aperture Radar (InSAR) prior to June 2018, and at an accelerated rate thereafter (Walter et al., 2019). Fissure development and fumarolic activity within the pyroclastic cone supports these observations of gradual deformation (Hunt et al., in press).

On 22 December 2018, plumes extending into the cloud base were observed from 14:30, with pulsatory Strombolian explosions peaking at 18:30 and a white plume descending to the shoreline, implying lava effusion (Perttu et al., 2020). The same authors report that fishermen decided the island was too dangerous to return to after

19:00 and observed lightning in the Strombolian plume at 20:00; and that two high-frequency seismic signals between 19:50 and 20:00 are consistent with small-scale slope failures. In the hour before the collapse, Darwin Volcano Ash Advisory Centre (VAAC) registered a final pre-collapse plume at 20:10 (Perttu et al., 2020). A cessation in audible explosions in the 30 minutes before the collapse broadly coincides with an infrasound signal pause of a few minutes (Walter et al., 2019), suggesting a pre-collapse break in surface activity (Perttu et al., 2020).

The main collapse occurred in a single stage of movement as indicated by tsunami observations and modelling (Grilli et al., 2019; timed at 20:55-57), eyewitness accounts (Perttu et al., 2020), as well as seismic (20:55:49) and infrasound signals (20:55:51) (Walter et al., 2019; Perttu et al., 2020; Ye et al., 2020; all consistent with a SW-moving landslide source). There is no evidence for an unusually large explosion preceding collapse (Perttu et al., 2020), although the main failure is bracketed by relatively high-frequency infrasound signals, two minutes before and 1.5 minutes afterwards. The former, at 20:54, is also observed in seismic records; Walter et al. (2019) interpret it as a possible explosion or earthquake signal that may have triggered the main collapse, whereas Perttu et al. (2020) conclude that it is consistent with a smaller-scale slope failure.

A brightness temperature reduction from Himawari-8 satellite data (11.2 µm channel) at ~20:55 indicates a volcanic cloud reaching ~16 km, coincident with the collapse (Gouhier and Paris, 2019; Perttu et al., 2020). This signal has a sharp onset and peaks at ~21:00, forming an ice-rich but ash-poor cloud advected to the SW (Prata et al., 2020) with ash emission lasting ~40 minutes (described as a blast-like explosion by Gouhier and Paris, 2019). Gouhier and Paris (2019) derive a higher mass-eruption rate for this specific plume (9×10^5 kg/s) than for the subsequent sustained phase (5 × 10^5 kg/s). Perttu et al. (2020) identify two further discrete explosive pulses at 22:25 and 22:55, progressing into sustained activity until 12:05 on 28 December. This supports gradual development of an ice-rich convective plume from 22:30, identified by Prata et al. (2020), reaching sustained levels by 01:00 on 23 December, at heights of 16-18 km. The SW ice-rich plume formed above an ash-laden weak column, generated by intense Surtseyan eruptions that advected eastwards at low altitudes (documented in aerial photographs on 23 December; Grilli et al., 2019; Prata et al., 2020; Hunt et al., in press). This low-altitude, ash-rich plume deposited tephra on Panjang island, 2 km east of Anak Krakatau (Fig.1), causing severe vegetation damage, with fine ash reaching the Javan coast (authors' observations). Intense Surtseyan activity lasted for two weeks, divided into three phases by Gouhier and Paris (2019) (22-27 December, 28-29 December, 3-6 January 2019) and two phases by Perttu et al. (2020) (22-28 December; 30 December to early January 2019).

Current observations, outlined above, demonstrate that the pre-collapse eruptive activity was intense but not unusual. There is no evidence of activity strongly accelerating in the hours before the collapse; behaviour on 22 December represented a renewal of vigorous eruptions, but output had peaked three months beforehand. A powerful explosive eruption accompanied the collapse, and was distinct from the sustained activity that followed within a few hours, with infrasound signals, satellite observations and aerial photographs suggesting an immediate switch from Strombolian to Surtseyan behaviour as water infiltrated the vent.

3. Tephra deposits

Ash samples (Supplementary Table 1) were collected from four different localities on Panjang and Sertung, islands respectively east and west of Anak Krakatau (Fig.1b). Difficulties with accessing higher ground meant that only one sample was collected from Sertung, at site U23-2 (6.38 km SW of the vent) (Fig.1c). This was collected in healthy forest, on level ground, at a ~100 m altitude and beyond the tsunami inundation limit. The dark volcanic ash sample was found at the surface as a 1-cm thick structureless layer mixed with leaf litter and above an organic soil, consistent with a fall deposit. U23-2 is in line with the south-westward dispersal of the high-level, ice-rich plume described above, but not with the NE/E-advected low-level plume. Visual and satellite observations show no evidence of post-collapse vegetation damage on Sertung. In contrast, significant ash deposition stripped leaves and branches from the mature forest on Panjang (S.1), consistent with observations of ash-laden plumes drifting over the island for several days after the collapse. Samples were collected at multiple sites on Panjang, displaying a well-bedded ash stratigraphy consistent with fall deposition, exceeding 20 cm in places (excluding remobilised surface deposits). At site U10, a flat, open area ~50 m from the shore on north Panjang, estimated to lie ~5 m above high-tide level, and 4.09 km from the vent, these deposits directly overlie a pumice-rich sand layer mixed with sparse marine shells, deposited on top of an organic soil (Fig.1a). A comparable ash stratigraphy was observed and sampled at other sites across Panjang (S.2), but with the pumice layer absent.

Samples from U23-2 and U10 were selected for further textural and geochemical analysis. All analytical methods are described in Appendix 1. For comparison, an older ash sample (KRA-233), from a May 1997 eruption, was also analysed, and was collected from a fall deposit on Sertung (Fig.1b), 3.80 km from the vent.

4. Results

4.1. Physical overview of eruptive products

The physical features (i.e. grain size, componentry, grain exterior surfaces) of the 1997 ash (KRA-233) provide an insight into the products of pre-collapse (Strombolian) magma ascent and fragmentation conditions, which can be contrasted with the December 2018 samples (Fig.1a and c) to evaluate changes in eruptive behaviour. KRA-233 is a poorly sorted ash (1.2 ϕ) with a unimodal grain size distribution peak of 2-3 ϕ and a fine ash content of 13% (>4 ϕ or <63 μm; Wohletz, 1983). The ash grains are predominantly glassy, black and angular (see Supplementary Table 2 for component descriptions).

U23-2 is a 1 cm thick, structureless and poorly sorted (1.2 ϕ) fine ash-fall deposit with a unimodal grain size of 2-3 ϕ. The deposit comprises highly glossy, fresh glassy grains, which are angular and have fluidal, frothy or pitted surface textures. These juvenile clasts can be divided into black and brown types; the latter are more open-textured, and this clast type is rare in KRA-233, in contrast with all 2018 samples. The unimodal characteristics and homogeneous physical appearance of U23-2 suggests it is the product of a single depositional event, rather than an amalgamated deposit from pre- or post-collapse activity (i.e. an upwind equivalent of the Panjang Surtseyan deposits). The high angularity (Fig.2d) and narrow grain-size range of U23-2 contrasts with the U10 samples (Fig.1a and c), as do several characteristics discussed in later sections.

U10 is a well-stratified sequence that lies beneath a >6-cm thick structureless surface layer of remobilised ash (U10-11) and can be subdivided into 8 distinct ash units (some comprising multiple layers; U10-3 to U10-10, with a total thickness of 21 cm overlying a pumiceous unit (U10-2). The ash units are characterised by moderate to poor sorting (0.9-1.6 ϕ) and unimodal grain-size peaks at 2-3 ϕ with a fine ash content ranging from ~8 to 33%. At the base of U10 (U10-1), a black structureless organic soil, rich in ash and rootlets, is inferred to derive from pre-2018 Anak Krakatau activity. The overlying unit, U10-2, is poorly sorted (1.4 ϕ), structureless and marked by erosional contacts with a maximum thickness of 11 cm. Sub-angular/sub-rounded cream pumice fragments dominate the layer (52%), and are assumed to originate from the 1883 Krakatau eruption based on appearance (cf. Carey et al., 2001). U10-2 also contains minor (<4%) marine biogenic material (e.g., gastropod shells, sponge spicules) (Fig.2c). Based on these characteristics and an absence of this layer at more elevated sites further inland (i.e., NP1 and NP2; S.2), U10-2 is interpreted as a tsunami deposit resulting from the 2018 landslide. U10-3 (U10-3A and -3B) is a thin (0.5 cm) and slightly indurated purple ash with an oxidised yellow-brown crust, distinct in colour and with by far the highest proportion of altered and lithic grains (Fig.2e; Supplementary Table 2) of any studied samples. U10-3 is also the only U10 unit that can be well-correlated, based on its distinctive colour, with other 2018 ash exposures on N Panjang (i.e., NP2-1; S.2). Above this, U10-4 is an inverse graded, planar bedded brown ash (35 mm) with a very fine top. Like U23-2, this ash is dominated by black and brown juvenile clasts, but these have a duller and less angular appearance. Grain characteristics are similar throughout the overlying sequence. Above U10-4, U10-5 (25 mm) and U10-6 (28 mm) are very fine (modal peak, 3-4 ϕ) brown ash beds, distinct from the rest of the sequence in displaying weak cross-stratification that becomes more developed near the top of the layers; we infer these may reflect deposition from basal surges rather than fallout. U10-7 to

U10-10 return to parallel planar bedded structures (Fig.1a). U10-7 (black medium ash; 25 mm) and U10-8 (a similar deposit; 4 mm) show slight normal grading and U10-9 (27-55 mm in total; up to 10 individual beds on a few-mm scale) and U10-10 (a 2 mm very fine basal brown ash overlain by three normally graded beds; 32 mm) display alternate fine and very fine ash size grades. Based on its multi-bedded characteristics and aerial observations of N/NE-directed ash-rich plumes (PVMBG, 2018; Prata et al., 2020), we infer that the U10-3 – U10-10 sequence represents deposition from pulsatory post-collapse Surtseyan activity between 22 December and early January 2019, though we cannot correlate exact dates with individual layers.

4.2. Exterior surfaces of grains

Scanning electron microscope (SEM) secondary-electron images of mounted ash grains were used to examine micro-scale features and potential differences in fragmentation modes between samples. Many grains from all samples display brittle features including stepped (Fig.2g) and conchoidal fractures, as well as river-line patterns that indicate fracturing under mixed-mode stresses (Hull, 1999). Additionally, many grains in U23-2 and U10 have secondary minerals (e.g., cubic NaCl) and/or finer particles adhered to their surfaces; in some cases, these finer particles have annealed together, creating irregular moss-like grains (Fig.2f; Büttner et al., 2002). There are also infrequent occurrences (~1%) of ductile features in U23-2 and U10 including Pele's hairs, platy grains, fluidal grains, and grains with molten surfaces. A notable feature of U23-2 is the presence of smooth glass spherules (cf. Genareau et al., 2015), which are not observed in the U10 or KRA-233 samples.

4.3. Ash morphology

Additional morphological and textural analyses of ash grains were undertaken on SEM backscattered-electron images of samples. Liu et al. (2015a) determined that proportions of dense (i.e. vesicle-poor grains, free crystals and lithics) and bubbly grains (vesicular grains/glass shards) can be distinguished using a concavity index (CI) threshold when plotting axial ratio against CI (Fig.3). Concavity index combines solidity (solidity = grain area/grain convex hull) and convexity (convexity = convex hull perimeter/grain perimeter) parameters, while axial ratio compares the major and minor axes of the grains' best fit ellipse (Liu et al., 2015b).

U23-2 displays a high proportion of dense grains (79%) to bubbly grains, averaged across three size fractions (250 -180 μm; 180 - 125 μm; 125 - 63 μm), characterised by a low concavity index (CI <0.4) (Fig.3a). The dominance of planar, fractured grains supports the high angularity observed from macrocomponentry of U23-2. By comparison, U10-3B and U10-4 (the lowermost 2018 Panjang deposits) have a very different morphology, with higher proportions of bubbly (75 and 70%, respectively) to dense grains across the size fractions (Fig.3b and c). There are slight variations between different size fractions: in U10-3B, the proportion of bubbly grains decreases with size, whereas the CI peaks in the 125-180 μm size fraction of U10-4, which may represent higher glass shard content (Liu et al., 2015a). Morphometric analysis of multiple grain size fractions was not undertaken for other units. However, data from U10-10 (63-125 μm size fraction) suggest comparable features to U10-3B and U10-4, and visual observations throughout the U10 sequence imply little variation in physical characteristics.

4.4. Whole-rock and groundmass glass compositions

Both bulk rock (X-ray fluorescence) and groundmass glass (electron probe microanalysis (EPMA)) compositions are summarised in Supplementary Table 3. U23-2 and all analysed U10 samples have a basaltic andesite bulk composition (SiO_2 = 54.1–55.4 wt.%, NaO + K_2O = 4.3–4.4 wt.%), maintaining the chemical homogeneity of older (1993 to 2017; Gardner et al., 2013) and pre-collapse deposits (July 2018; Walter et al., 2019) (SiO_2 = 54.0–55.8 wt.%, NaO + K_2O = 4.2–4.6 wt.%). The only unit that displays a subtle difference is U10-3, which has a slightly higher loss on ignition value and elevated SO_3 and Cu contents. Along with its discolouration and lithic abundance (Fig. 2e), this may reflect a higher proportion of hydrothermally altered material in this Surtseyan deposit than later units.

Matrix glass compositions (S.3) between KRA-233 (the 1997 ash) and U23-2 are indistinguishable (mostly within the range SiO_2 = 59.0–61.0 wt.%), but those in the U10 sequence are slightly less evolved with a narrow andesite compositional range (SiO_2 = 58.0–60.5 wt.%).

4.5. Phase assemblage

EMPA and SEM analyses show that all studied samples contain a microlite (<50 µm in size), microphenocryst (~50 µm-0.5 mm in size) and phenocryst (~0.5-1 mm in size) assemblage of plagioclase, orthopyroxene, olivine, clinopyroxene and titanomagnetite within a glassy silicate matrix.

Plagioclase is the most abundant phase (~10 to 26 % area) in all samples, forming subhedral to euhedral phenocrysts and microphenocrysts. Both phenocryst types display normal or reverse zoning, resorbed and sieve textures, and amoeboid melt inclusions. Plagioclase microlite morphologies in KRA-233 and U23-2 are dominantly tabular, with rare swallow-tail and skeletal forms observed in U23-2. The

U10 samples contain a wider variety of morphologies including tabular, acicular, skeletal, hopper and swallow-tail forms (Fig.4). Moreover, numerous feldspar microlites in U10 are surrounded by a thin Fe-Ti rich compositional boundary layer (Fig.4e), formed only when plagioclase growth rates match or exceed diffusion rates in adjacent melt (Honour et al., 2019). KRA-233 and U23-2 microlites share a similar compositional range of An_{48} to An_{68} (An, Anorthite = molar Ca/ (Ca + Na + K); mol %). In contrast, the microlites in the U10 samples extend to An_{79} (Fig.5a). Microlites in all samples display a common main peak at An_{56}, but U10 samples show two subsidiary peaks at An_{68} and An_{75}. Microphenocryst and phenocryst core compositions for all samples are more primitive (i.e. more anorthitic; ranges of An_{62-91} and An_{45-89}, respectively) than corresponding rims (An_{48-68} and An_{51-79}, respectively). The rims also show more primitive compositions progressively higher up the U10 stratigraphy (U23-2 is also among the least primitive, but does not extend to anorthite contents as low as KRA-233); core compositions exhibit the same trend, albeit less strongly (Fig.5a). The range of anorthite contents is consistent with data from 1970-2002 lava flows (Camus et al., 1987; Dahren et al., 2012).

KRA-233 and U23-2 have minor proportions of mafic minerals (i.e., orthopyroxene, olivine, clinopyroxene and oxides) (areal mean ~<6%), whereas U10 samples contain nearly double the proportion of these minerals (areal mean ~11%). Pyroxene, olivine, and oxide phenocrysts and microphenocrysts in all samples are predominantly euhedral. Microlite morphologies are largely tabular, equant or skeletal. U23-2 is the only sample where polymineralic glomerocrysts (i.e., crystal aggregates of various phases) are observed. Orthopyroxene is more dominant than clinopyroxene, but both are heterogenous in composition, with orthopyroxene spanning the enstatite-pigeonite fields and clinopyroxene the pigeonite-augite fields

(Fig. 5c and d). The Mg# (Mg# = molar Mg/(Mg + Fe)) of orthopyroxene ($Mg\#_{66\text{-}74}$) and clinopyroxene ($Mg\#_{69\text{-}76}$) are homogeneous for core-rim pairs, with groundmass values generally falling below $Mg\#_{70}$, consistent with 1990-2002 lava flows ($Mg\#_{61\text{-}74}$, opx; $Mg\#_{73\text{-}77}$, cpx; Dahren et al., 2012). Forsterite content (Fo = molar Mg/(Mg + Fe); mol %) of olivine in phenocryst core-rim pairs ($Fo_{69\text{-}80}$) and microlites ($Fo_{66\text{-}73}$) for the U23-2 and U10 samples are slightly more primitive than in rocks erupted in the 1970s (Camus et al.,1987) and KRA-233 ($Fo_{56\text{-}68}$, microlites; $Fo_{62\text{-}73}$, cores and rims) (Fig.5b).

4.6. Microtextural observations

The U23-2 and U10 samples display distinct stratigraphic differences in the 2D analysis of feldspar populations (Fig.6; S.4). All 2D textural data are summarised in Table 1. Plagioclase areal number density (N_A), which defines the number of feldspars per unit area (mm^{-2}), is lowest in the 1997 KRA-233 sample (11,194 mm^{-2}). N_A in U23-2 is also relatively low (12,062 mm^{-2}), whereas U10-4, early in the post-collapse Surtseyan sequence, has the highest density (44,545 mm^{-2}). U10-3 (both U10-3A and B) is slightly lower than U10-4, and later U10 samples range between 13,342 and 37,969 mm^{-2}.

Plagioclase microlite crystallinity (φ) describes the fraction that feldspar microlites occupy within the groundmass, excluding all vesicles, phenocrysts, and pyroxene and Fe-Ti oxide microlites (Hammer et al., 2000). A plot of N_A versus φ reveals that U23-2 and KRA-233 have similar characteristics (S.5). Later U10 samples are also similar but with slightly higher N_A and lower φ, while U10-4 and, to a lesser extent, U10-3A/B show much higher values of both parameters (S.5). The mean crystal sizes (S_n) of all samples range from ~2.56 to 4.56 µm, with the smallest crystals in

U10-3B and the largest crystals in U23-2. A negative correlation is evident between N_A and S_n, indicating that samples either have high numbers of small microlites or the reverse (S.5). Feldspar aspect ratios for U10-4, U10-6, U10-8 and U10-10 are high (5.14 – 7.28), representing more elongated crystal habits, whereas KRA-233, U23-2 and U10-3A/B have lower ratios (4.08 – 4.19), defining more tabular crystals.

Vesicle morphologies within grains vary depending on crystallinity. Microlite-poor grains typically exhibit smaller, spherical, and isolated vesicles, whereas microlite-rich grains contain irregular and coalesced vesicles.

4.6.1. Ascent rates

To assess approximate ascent rates, we used the microlite number density (MND) exsolution rate meter of Toramaru et al. (2008). Although this explicitly relates to microlite nucleation depths, it likely reflects a time-averaged ascent rate throughout the conduit (Murch and Cole, 2019). Since we used vesicular, microlite-rich grains, the textures reveal ascent conditions near the conduit walls, providing longer residence times for microlite crystallisation (Taddeucci et al., 2004). Therefore, ascent rates may be considered as minimum values. The main equations from Toramaru et al. (2008) are summarised here. Decompression rates (dP_w/dz) are estimated by:

$$\left|\frac{dP_w}{dz}\right| = \frac{c}{b}\left(\frac{Nv}{a}\right)^{\frac{2}{3}} \quad (1)$$

where *b* represents a constant (40 for plagioclase), *c* is a function of water content (C_w), N_v is microlite number volume, and *a* is a calculation involving C_w and glass silica content (C_{Si}). Microlite water content was estimated using the plagioclase-melt hygrometer of Putirka (2008), with values ranging between 2.5 and 3.6 ± 1 wt.% for all samples (akin to Dahren et al., 2012). Magmatic ascent velocities (V_n) can then be calculated using the decompression rate:

$$V_n = \frac{1}{\rho g}\left|\frac{dP_w}{dz}\right| \tag{2}$$

where ρ is the density of vesiculated magma (estimated using porosity values from ImageJ analysis and a 2700 kg m^{-3} magma density), g is gravity, and dP_w/dz is the decompression rate at the nucleation depth of feldspar microlites.

KRA-233, the 1997 Strombolian ash, yields a relatively low mean ascent rate of 1.04 m s^{-1}. This is similar but slightly higher than that of U23-2, with a mean rate of 0.76 m s^{-1}. Early U10 samples show sharply elevated mean values of ~2 m s^{-1} for U10-3, increasing to 4.45 m s^{-1} for U10-4 and then dropping to lower ascent rates for later U10-samples (0.99-1.84 m s^{-1}) (Fig.6).

5. Discussion

5.1. Timing of initial deposits

Bulk magma compositions at Anak Krakatau from 1993 to 2018 show negligible changes (Gardner et al., 2013; Walter et al., 2019), implying no compositionally different magma input associated with the 2018 lateral collapse. This corresponds with observations that pre-collapse activity was typical of previous eruptions, despite increased intensity (Perttu et al., 2020). Nonetheless, our textural and mineralogical observations reveal that U23-2 is distinct from the U10 sequence, while early U10 deposits (U10-3 and U10-4) also differ slightly from overlying units. U23-2 contrasts with U10 (Panjang post-collapse deposits) morphologically, in its predominance of highly angular, dense clasts; it is also less primitive in terms of both glass and mineral compositions, and its microlite crystallinity and estimated mean ascent rate are consistent with relatively slow processes, broadly corresponding with pre-collapse Strombolian conditions (i.e., KRA-233, the 1997 ash). The overall homogeneity of U23-2 in its deposit- and grain-scale characteristics suggests that it cannot be an upwind equivalent of U10, implying derivation from a discrete event. We thus interpret U23-2 as a deposit from the initial explosive pulse that accompanied the lateral collapse at ~20:55, involving the most intense mass eruption rate in the collapse period (Gouhier and Paris, 2019), its plume reaching 16 km in altitude and transported SW (e.g. Prata et al., 2020). This ‘syn-collapse’ explosion lasted ~40 minutes (Gouhier and Paris, 2019). The resulting 1-cm thick deposit on Sertung indicates that although this plume was relatively ash-poor, it was distinct from the ash-depleted, ice-dominated convective plumes sustained over the following days (Prata et al., 2020). The presence of glass spherules, observed only in U23-2 (cf. Genareau et al., 2015), is consistent with material derived from a lightning-rich column (Fig.2f) (a notable feature of the high-level SW plume; Prata et al., 2020).

The U10-2 tsunami deposit also provides an important time constraint for the Panjang deposits. Tsunami simulations suggest that maximum wave inundation at U10 occurred ~6.3 minutes after the collapse (S.2c). Our interpretation would suggest that U23-2 and U10-2 were deposited broadly synchronously, and if U23-2 was derived from the high level syn-collapse plume it may have an equivalent deposit on Panjang. On Panjang, such a deposit would be thin (given its upwind position) and potentially mixed with or eroded by the U10-2 tsunami deposit. We found no evidence of U23-2-type clasts within U10-2, and not did we find evidence of a discrete U23-2-type layer beneath the basal purple ash at other sites on Panjang. Any such layer would likely be very thin and difficult to distinguish from the underlying ash-rich soil, and we are thus unable to provide any further constraints on the relative timing and depositional pattern of these various units.

5.2. Unloading effects on microlite textures

Edifice destruction causes an instantaneous pressure drop in the underlying magmatic system (Pinel and Jaupart, 2005), which may be manifested in microlite textures that reveal decompression conditions during ascent (e.g., Preece et al., 2013). Variable microlite textures can be attributed to changes in effective undercooling (ΔT, defined as $T_{liquidus} – T_{magma;}$ Crabtree and Lange, 2011) during crystallisation. Low ΔT and slow decompression produces fewer and larger crystals, developing under a crystal growth-dominated regime. In contrast, a nucleation-dominated regime arises at higher ΔT and faster decompression, forming numerous smaller microlites (e.g., Mollo and Hammer, 2017). Our samples can be divided into three phases that span the collapse. Phase A is recorded by U23-2, representing a crystal growth-dominated process, displaying the lowest areal microlite number density (N_A), more tabular microlites, and the largest mean microlite size (Lofgren, 1980). The textural similarities of U23-2 and KRA-233 suggest both samples record steady-state conditions characteristic of the Strombolian feeder system up until the point of collapse (Fig. 7a), with relatively low ascent and decompression rates. U23-2 is thus essentially recording the imprint of pre-collapse ascent and crystallisation conditions. The absence of textural disequilibrium in U23-2 suggests that, texturally, it does not record a pressure perturbation associated with collapse, and that it therefore represents magma within the surficial portion of the conduit. Its fragmentation would then be a direct consequence of decompression, as a blast-like response to edifice failure (e.g. Alidibirov and Dingwell, 1996). This notion of 'conduit clearing' is consistent with the timing and short-lived nature of the initial explosive pulse (Gouhier and Paris, 2019; Perttu et al., 2020; Prata et al., 2020), which is indistinguishable from the timing of the collapse itself.

The U10-3 and U10-4 deposits represent Phase B, with a sharp increase in N_A and crystallinity, smaller mean microlite sizes, higher aspect ratios, and various disequilibrium morphologies, implying nucleation-dominated crystallisation under high ΔT (Lofgren, 1980). The abundance of acicular, hopper and swallow-tail morphologies in the U10 samples affirm high decompression rates and undercooling (Hammer and Rutherford, 2002; Couch et al., 2003). Rapid degassing associated with open-system decompression of the conduit following collapse may explain the sharp change in crystal development, as $T_{liquidus}$ (and ΔT) would have increased through both decompression and water loss (e.g., Cashman and Blundy, 2000). Destabilisation of a pressurised conduit during the collapse, further unloaded by the initial explosive pulse of U23-2, may have facilitated the rapid acceleration of deeper magma, evident in the increasing ascent rates (and increasing evidence of disequilibrium microlite textures) estimated for U10-3 and U10-4. Rapid, decompression-induced crystallisation of early U10 samples is further supported by high pyroxene and titanomagnetite microlite proportions (Fig.4c and d), as decompression experiments indicate pyroxene and oxide content increases under higher decompression (Szramek et al., 2006).

Finally, Phase C is represented by later U10 samples (U10-6, U10-8 and U10-10), which indicate a general decrease in N_A and crystallinity, and an increase in mean microlite size, consistent with a gradual re-stabilisation of the feeder system with reduced magma ascent velocities.

5.3. Effects of collapse on mineral chemistry

Mineral compositions are sensitive to changes in temperature, pressure, and volatile content. Differences in plagioclase anorthite-content between U23-2 and U10 support the above textural interpretation, with U10 groundmass compositions (Phase B and C) extending to notably higher values (An_{67-79}) than U23-2 (Phase A), with a discrete calcic population indicative of relatively higher water pressures and temperatures (Fig.5a) (Couch et al., 2003). This could correspond with derivation as entrained crystals from deeper in the plumbing system, since the main microlite population in all samples spans a comparable compositional range (An_{50-63}) consistent with crystallisation extending to shallow levels. Plagioclase phenocryst rims exhibit increasing An-content higher up the U10 stratigraphy (Fig.5a), suggesting that most plagioclase crystals equilibrated under differing physio-chemical conditions in each sample and/or were in disequilibrium with the compositionally homogenous melt (S.3) (Petrone et al., 2009). Last-equilibrated depths can be estimated from EPMA data using plagioclase-melt and orthopyroxene-melt barometers (Putirka, 2008) (Supplementary Table 4). Considering the K_D crystal-melt equilibrium criterion (Putirka, 2008; for both plagioclase and orthopyroxene, using average matrix glass compositions), many phenocryst rim compositions fail to meet the threshold. However, from the limited usable dataset (n=17), calculated depths (using densities 2320-2800 kg m^{-3}; Kopp et al., 2001) are consistent with previous upper crustal estimates (e.g. Dahren et al., 2012), indicating two main levels at ~4-7 km (plagioclase) and 8-12 km (plagioclase and orthopyroxene). Plagioclase phenocryst core compositions are relatively similar across U23-2 and U10, but more anorthitic than those in the 1997 magma (KRA-233). This implies that all the magma erupted in 2018 can be considered a related batch, even if microlite compositions record an overprint of variable ascent conditions. This is also supported by olivine and pyroxene phenocryst core compositions, based on a more limited dataset (Fig. 5b, c, d).

5.4. Fragmentation and magma-water interaction

Ash morphological and surface characteristics in the U23-2 and U10 samples indicate variation in fragmentation modes caused primarily by two brittle mechanisms. The vitric nature, fracture patterns and high angularity of U23-2 relative to U10 (Fig. 2d and e) correspond with the sudden effect of rapid decompression; angularity resulting from a top-down propagating decompression wave, producing brittle fracture and relatively denser textures (Alidibirov and Dingwell, 1996). In U10, blocky and sub-angular morphologies, alongside stepped or river-line fractures on grain surfaces, also signify a dominant brittle fragmentation process. However, the overall increase in vesicularity relative to U23-2 (Fig.3b and c) suggests this was driven by vesicle overpressure, facilitated by rapid ascent and extensive degassing (Cioni et al., 2014; Gouhier and Paris, 2019). Minor ductile features (i.e. Pele's hairs) also emphasise the melt's relatively low viscosity, exiting the vent at high velocity (Büttner et al., 2002).

Visual observations and infrasound signals indicate the onset of Surtseyan activity after the collapse (Perttu et al., 2020). Interaction with seawater, leading to further brittle and ductile fragmentation, may have overprinted the primary brittle mechanisms (cf. Liu et al., 2017), although we would expect this to be more limited in U23-2. The high lithic and altered grain content in U10-3 (and NP2-2; S.2) suggests a vent widening stage that enabled greater magma-water interaction, following the unloading-induced explosion of U23-2. Finer tails in the U10 grain-size distributions compared to U23-2 (Fig.1a) may reflect a greater fragmentation efficiency following this vent reconfiguration. Furthermore, the collapse not only exposed the vent to seawater, but also uncovered the subsurface hydrothermal system beneath the SW flank, indicated by the orange seawater plumes evident days after the collapse (S.1b). Excavation of the hydrothermally altered edifice by Surtseyan activity, during the vent widening stage, is apparent from the distinct colouration and chemistry of U10-3.

5.5. Reconstruction of syn- and post-collapse eruptive activity

Immediately after Anak Krakatau's collapse at ~20:55, decompression initiated brittle fragmentation of magma in the shallow conduit, which had been feeding Strombolian eruptions and had ascended under conditions characteristic of the preceding months (Fig.7a). This elicited a highly explosive and short-lived eruption (Phase A), with rapid plume ascent reaching ~16 km (Gouhier and Paris, 2019; Prata et al., 2020) (Fig.7b). Phase A marked the onset of elevated open-system degassing, with SO_2 output from 22 to 28 December estimated at ~98 kt (Gouhier and Paris, 2019).

During Phase B, extensive degassing coupled with rapid decompression and tapping of the deeper feeder system, shifted the crystallisation regime towards rapid nucleation of smaller microlites. U10-3 defines the onset of extensive seawater interaction, with a vent widening stage leading to typical Surtseyan activity, producing cock's tail jets and ash-laden low-altitude plumes (Fig.7c) (Prata et al., 2020). Increasing magma ascent rates and vesicularity suggest primary brittle fragmentation driven by vesicle overpressure.

In Phase C, magma ascent conditions gradually stabilised, in response to pressure conditions that had been modified both by the collapse and then by the rapid island regrowth that accompanied the post-collapse eruptions (Fig.7d). Magma ascent rates exhibit progressively slower velocities, and degassing reduced by nearly 50% in late December and by 75% in early January 2019 (Gouhier and Paris, 2019). Given the very rapid regrowth (cf. Hunt et al., in press), we suggest that the volcano returned to equilibrium conditions (i.e., potentially comparable with the pre-collapse storage state) within a 1-2 week period as activity waned.

5.6. Implications for determining future collapse events and collapse impacts

As there is no evidence for elevated/unusual magma ascent patterns immediately preceding the collapse, it is unlikely that any distinctive magmatic (i.e., volcano seismicity, inflation or degassing) signatures would have been apparent that could have indicated incipient collapse. However, progressive susceptibility of the SW flank to failure was evident from longer-term deformation and growth patterns. Slow lateral deformation of the failed SW flank was identified over 10 years before the collapse (Agustan et al., 2012; Chaussard and Amelung, 2012), with evidence of an increase in the 2018 eruptive period (Walter et al., 2019). Since longer-term deformation datasets are limited, it is difficult to assess whether deformation rates in 2018 were substantially different to those during previous eruptions, or whether displacements showed an overall accelerating pattern. Nonetheless, longer-term patterns of Anak Krakatau's edifice growth reflect significant structural instabilities, including the volcano's position on the scarp of the 1883 Krakatau caldera (Deplus et al., 1995); pre-1960 asymmetrical growth of the tuff cone towards the NE, and post-1960 vent migration facilitating SW emplacement of lava deltas (cf. Hunt et al., in press). While eruptions do not always trigger edifice instability, the June-December 2018 activity itself is also likely to have played a role in the timing of the collapse by increasing flank loading and potentially increasing pressurisation in the subsurface hydrothermal system (e.g., Reid, 2004). All these instabilities, combined with the 2018 eruptive activity, ultimately pre-conditioned the SW flank for its eventual collapse. For future monitoring of edifice stability at Anak Krakatau or elsewhere, an approach integrating short- and long-term edifice growth patterns with flank deformation monitoring (cf. Gonzalez-Santana and Wauthier, 2020), and an improved understanding of edifice material properties, may hold the best prospects for refining forecasts of collapse timing.

The Anak Krakatau collapse also reveals the impact of surface-unloading driven disruption on a shallow magmatic system. Although the collapse volume was small relative to historical collapses (e.g., Ritter Island; Karstens et al., 2019), sudden decompression led to a considerable magmatic response and readjustment, causing highly elevated eruption rates. This elevated magma flux rapidly infilled the landslide scar and extended the island coastline (e.g., Novellino et al., 2020; Hunt et al., in press). This highlights that temporarily high post-collapse eruption rates may hinder opportunities to identify and investigate collapse processes by concealing failure scars and stratigraphic records of collapse-associated activity (e.g., Watt, 2019).

6. Conclusions

Our physical, microtextural and geochemical analysis of syn- and post-collapse deposits shows no evidence that a change in magmatic conditions or eruptive behaviour preceded the lateral collapse of Anak Krakatau. Instead, the intense, accompanying volcanism is interpreted as a response to collapse and can be divided into three main phases. Phase A involved a syn-collapse eruption triggered by collapse-driven decompression of the shallow conduit, generating a powerful explosive pulse and depositing ash to the SW. Textures in this ash record pre-collapse ascent conditions, excluding a direct magmatic trigger for the collapse, and suggesting the collapse resulted from structural and gravitational instabilities arising from patterns in edifice development.

Post-collapse eruptive activity in Phase B reflects deeper tapping of successive magma batches from the depressurised conduit, with extensive degassing and accelerating ascent rates. Gradual re-stabilisation of conduit conditions occurs in Phase C, as rapid edifice regrowth led to waning activity.

The 2018 collapse highlights that lateral collapses are not necessarily directly triggered by immediate shifts in magmatic behaviour, which standard monitoring techniques could have potentially detected. Therefore, effective volcanic monitoring and forecasting of such collapse events may need to focus on identifying areas with increased susceptibility to failure, as signalled by changing edifice growth patterns and flank deformation; this will be particularly relevant for the future growth of Anak Krakatau.

Acknowledgements

We thank Alastair Hodgetts, Thomas Williams and Daniel Cox for help with sample preparation, Victoria Smith and Stuart Kearns for assistance with the electron microprobe, and Gren Turner for assistance with the SEM. This work was supported by NERC Grant NE/T002026/1 (SFLW, MC, SLE, MB). SFLW, SLE, DRT also acknowledge funding from NERC grant NE/S003509/1. MC acknowledges NERC fellowship NE/N014286/1. ALMN acknowledges NERC studentship NE/L202612/1.

MA acknowledges MAIPARK Research Grant. CH acknowledges funding from NERC grant NE/S004106/1 and COMET (https://comet.nerc.ac.uk/). JEH would like to acknowledge funding from NERC Grant NE/T002034/1. SLE, DRT and AN publish with the permission of the CEO, British Geological Survey.

References

Abdurrachman, M., Widiyantoro, S., Priadi, B. and Ismail, T., 2018. Geochemistry and Structure of Krakatoa Volcano in the Sunda Strait, Indonesia. *Geosciences*, *8*(4), p.111.

Agustan, Kimata, F., Pamitro, Y.E. and Abidin, H.Z., 2012. Understanding the 2007–2008 eruption of Anak Krakatau Volcano by combining remote sensing technique and seismic data. *International Journal of Applied Earth Observation and Geoinformation*, *14*(1), pp.73-82.

Alidibirov, M. and Dingwell, D.B., 1996. Magma fragmentation by rapid decompression. *Nature*, *380* (6570), pp.146-148.

Büttner, R., Dellino, P., La Volpe, L., Lorenz, V. and Zimanowski, B., 2002. Thermohydraulic explosions in phreatomagmatic eruptions as evidenced by the comparison between pyroclasts and products from Molten Fuel Coolant Interaction experiments. *Journal of Geophysical Research: Solid Earth*, *107*(B11), pp.ECV-5.

Camus, G., Gourgaud, A. and Vincent, P.M., 1987. Petrologic evolution of Krakatau (Indonesia): implications for a future activity. *Journal of Volcanology and Geothermal Research*, *33*(4), pp.299-316.

Carey, S., Morelli, D., Sigurdsson, H. and Bronto, S., 2001. Tsunami deposits from major explosive eruptions: an example from the 1883 eruption of Krakatau. *Geology*, *29*(4), pp.347-350.

Cashman, K. and Blundy, J., 2000. Degassing and crystallization of ascending andesite and dacite. *Philosophical Transactions of the Royal Society of London. Series A: Mathematical, Physical and Engineering Sciences*, *358*(1770), pp.1487-1513.

Chaussard, E. and Amelung, F., 2012. Precursory inflation of shallow magma reservoirs at west Sunda volcanoes detected by InSAR. *Geophysical Research Letters*, *39*(21).

Cioni, R., Pistolesi, M., Bertagnini, A., Bonadonna, C., Hoskuldsson, A. and Scateni, B., 2014. Insights into the dynamics and evolution of the 2010 Eyjafjallajökull summit eruption (Iceland) provided by volcanic ash textures. *Earth and Planetary Science Letters*, *394*, pp.111-123.

Couch, S., Harford, C.L., Sparks, R.S.J. and Carroll, M.R., 2003. Experimental constraints on the conditions of formation of highly calcic plagioclase microlites at the Soufriere Hills Volcano, Montserrat. *Journal of Petrology*, *44*(8), pp.1455-1475.

Crabtree, S.M. and Lange, R.A., 2011. Complex phenocryst textures and zoning patterns in andesites and dacites: Evidence of degassing-induced rapid crystallization?. *Journal of Petrology*, *52*(1), pp.3-38.

Dahren, B., Troll, V.R., Andersson, U.B., Chadwick, J.P., Gardner, M.F., Jaxybulatov, K. and Koulakov, I., 2012. Magma plumbing beneath Anak Krakatau volcano, Indonesia: evidence for multiple magma storage regions. *Contributions to Mineralogy and Petrology*, *163*(4), pp.631-651.

Deplus, C., Bonvalot, S., Dahrin, D., Diament, M., Harjono, H. and Dubois, J., 1995. Inner structure of the Krakatau volcanic complex (Indonesia) from gravity and bathymetry data. *Journal of Volcanology and Geothermal Research*, *64*(1-2), pp.23-52.

Gardner, M.F., Troll, V.R., Gamble, J.A., Gertisser, R., Hart, G.L., Ellam, R.M., Harris, C. and Wolff, J.A., 2012. Crustal differentiation processes at Krakatau volcano, Indonesia. *Journal of Petrology*, *54*(1), pp.149-182.

Genareau, K., Wardman, J.B., Wilson, T.M., McNutt, S.R. and Izbekov, P., 2015. Lightning-induced volcanic spherules. *Geology*, *43*(4), pp.319-322.

Gonzalez-Santana, J. and Wauthier, C., 2020. Unraveling long-term volcano flank instability at Pacaya Volcano, Guatemala, using satellite geodesy. *Journal of Volcanology and Geothermal Research*, p.107147.

Gouhier, M. and Paris, R., 2019. SO2 and tephra emissions during the 22 December, 2018 Anak Krakatau eruption. *Volcanica*, *2*(2), pp.91-103.

Grilli, S.T., Tappin, D.R., Carey, S., Watt, S.F., Ward, S.N., Grilli, A.R., Engwell, S.L., Zhang, C., Kirby, J.T., Schambach, L. and Muin, M., 2019. Modelling of the tsunami from the 22 December, 2018 lateral collapse of Anak Krakatau volcano in the Sunda Straits, Indonesia. *Scientific reports*, *9*(1), pp.1-13.

Hammer, J.E., Cashman, K.V. and Voight, B., 2000. Magmatic processes revealed by textural and compositional trends in Merapi dome lavas. *Journal of Volcanology and Geothermal Research*, *100*(1-4), pp.165-192.

Hammer, J.E. and Rutherford, M.J., 2002. An experimental study of the kinetics of decompression-induced crystallisation in silicic melt. *Journal of Geophysical Research: Solid Earth*, *107*(B1). DOI: https://doi.org/10.1029/2001JB000281

Honour, V.C., Holness, M.B., Charlier, B., Piazolo, S.C., Namur, O., Prosa, T.J., Martin, I., Helz, R.T., Maclennan, J. and Jean, M.M., 2019. Compositional boundary layers trigger liquid unmixing in a basaltic crystal mush. *Nature communications*, *10*(1), pp.1-8.

Hunt, J.E., Tappin, D.R., Watt, S.F.L., Susilohadi, S., Novellino, A., Ebmeier, S.K., Cassidy, M., Engwell, S.L., Grilli, S.T., Hanif, M., Priyanto, W.S., Clare, M.A., Abdurrachman, M. and Udrekh, U., 2021. Submarine landslide megablocks show half of Anak Krakatau island failed on December 22nd, 2018. *Nature Communications*, in press.

Hull, D., 1999. *Fractography: observing, measuring and interpreting fracture surface topography*. Cambridge University Press.

Karstens, J., Berndt, C., Urlaub, M., Watt, S.F., Micallef, A., Ray, M., Klaucke, I., Muff, S., Klaeschen, D., Kühn, M. and Roth, T., 2019. From gradual spreading to catastrophic collapse–Reconstruction of the 1888 Ritter Island volcanic sector collapse from high-resolution 3D seismic data. *Earth and Planetary Science Letters*, *517*, pp.1-13.

Kopp, H., Flueh, E.R., Klaeschen, D., Bialas, J. and Reichert, C., 2001. Crustal structure of the central Sunda margin at the onset of oblique subduction. *Geophysical Journal International*, *147*(2), pp.449-474.

Liu, E.J., Cashman, K.V., Rust, A.C. and Gislason, S.R., 2015a. The role of bubbles in generating fine ash during hydromagmatic eruptions. *Geology*, *43*(3), pp.239-242.

Liu, E.J., Cashman, K.V. and Rust, A.C., 2015b. Optimising shape analysis to quantify volcanic ash morphology. *GeoResJ*, *8*, pp.14-30.

Liu, E.J., Cashman, K.V., Rust, A.C. and Höskuldsson, A., 2017. Contrasting mechanisms of magma fragmentation during coeval magmatic and hydromagmatic activity: the Hverfjall Fires fissure eruption, Iceland. *Bulletin of Volcanology*, *79*(10), p.68.

Lofgren, G.,1980. Experimental studies on the dynamic crystallisation of silicate melts. *Physics of magmatic processes*, p.487-551.

López, D.L. and Williams, S.N., 1993. Catastrophic volcanic collapse: relation to hydrothermal processes. *Science*, *260*(5115), pp.1794-1796.

McGuire, W.J., 2003. Volcano instability and lateral collapse. *Revista*, *1*, pp.33-45.

Mollo, S. and Hammer, J.E., 2017. Dynamic crystallization in magmas. *EMU Notes in Mineralogy*, *16*, pp.373-418.

Murch, A.P. and Cole, P.D., 2019. Using microlites to gain insights into ascent conditions of differing styles of volcanism at Soufrière Hills Volcano. *Journal of Volcanology and Geothermal Research*, *384*, pp.221-231.

Novellino, A., Engwell, S.L., Grebby, S., Day, S., Cassidy, M., Madden-Nadeau, A., Watt, S., Pyle, D., Abdurrachman, M., Edo Marshal Nurshal, M. and Tappin, D.R., 2020. Mapping recent shoreline changes spanning the lateral collapse of Anak Krakatau Volcano, Indonesia. *Applied Sciences*, *10*(2), p.536.

Perttu, A., Caudron, C., Assink, J.D., Metz, D., Tailpied, D., Perttu, B., Hibert, C., Nurfiani, D., Pilger, C., Muzli, M. and Fee, D., 2020. Reconstruction of the 2018 tsunamigenic flank collapse and eruptive activity at Anak Krakatau based on eyewitness reports, seismo-acoustic and satellite observations. *Earth and Planetary Science Letters*, *541*, p.116268.

Petrone, C.M., Braschi, E. and Francalanci, L., 2009. Understanding the collapse–eruption link at Stromboli, Italy: a microanalytical study on the products of the recent Secche di Lazzaro phreatomagmatic activity. *Journal of Volcanology and Geothermal Research*, *188*(4), pp.315-332.

Pinel, V. and Jaupart, C., 2005. Some consequences of volcanic edifice destruction for eruption conditions. *Journal of Volcanology and Geothermal Research*, *145*(1-2), pp.68-80.

Prata, A.T., Folch, A., Prata, A.J., Biondi, R., Brenot, H., Cimarelli, C., Corradini, S., Lapierre, J. and Costa, A., 2020. Anak Krakatau triggers volcanic freezer in the upper troposphere. *Scientific reports*, *10*(1), pp.1-13.

Preece, K., Barclay, J., Gertisser, R. and Herd, R.A., 2013. Textural and micro-petrological variations in the eruptive products of the 2006 dome-forming eruption of Merapi volcano, Indonesia: implications for sub-surface processes. *Journal of Volcanology and Geothermal Research*, *261*, pp.98-120.

Putirka, K.D., 2008. Thermometers and barometers for volcanic systems. *Reviews in mineralogy and geochemistry*, *69*(1), pp.61-120.

PVMBG, 2018. *Badan Geologi* [online]. Available at: https://vsi.esdm.go.id (Accessed: 3rd March 2019).
Reid, M.E., 2004. Massive collapse of volcano edifices triggered by hydrothermal pressurization. *Geology*, *32*(5), pp.373-376.
Siebert, L., Glicken, H. and Ui, T., 1987. Volcanic hazards from Bezymianny-and Bandai-type eruptions. *Bulletin of Volcanology*, *49*(1), pp.435-459.
Szramek, L., Gardner, J.E. and Larsen, J., 2006. Degassing and microlite crystallisation of basaltic andesite magma erupting at Arenal Volcano, Costa Rica. *Journal of Volcanology and Geothermal Research*, *157*(1-3), pp.182-201.
Toramaru, A., Noguchi, S., Oyoshihara, S. and Tsune, A., 2008. MND (microlite number density) water exsolution rate meter. *Journal of Volcanology and Geothermal Research*, *175*(1-2), pp.156-167.
Walter, T.R., Haghighi, M.H., Schneider, F.M., Coppola, D., Motagh, M., Saul, J., Babeyko, A., Dahm, T., Troll, V.R., Tilmann, F. and Heimann, S., 2019. Complex hazard cascade culminating in the Anak Krakatau sector collapse. *Nature communications*, *10*(1), pp.1-11.
Watt, S.F.L., 2019. The evolution of volcanic systems following sector collapse. *Journal of Volcanology and Geothermal Research*, 384, pp. 280-303.
Wohletz, K.H., 1983. Mechanisms of hydrovolcanic pyroclast formation: grain-size, scanning electron microscopy, and experimental studies. *Journal of Volcanology and Geothermal Research*, *17*(1-4), pp.31-63.
Ye, L., Kanamori, H., Rivera, L., Lay, T., Zhou, Y., Sianipar, D. and Satake, K., 2020. The 22 December 2018 tsunami from flank collapse of Anak Krakatau volcano during eruption. *Science Advances*, *6*(3), p.1377.

Figure captions

Figure 1

U10 and U23-2 stratigraphic sections and grain size data. **a** The physical characteristics of the U10 sequence on northern Panjang (image, sedimentary log and grain size distributions (sieved and laser diffraction data)). **b** Inset map showing location of Anak Krakatau and sample localities (main sites of U23-2 and U10 = yellow circles; additional sites of NP1 and NP2 = dark blue pentagons). **c** The physical characteristics of U23-2 from southern Sertung (sedimentary log and grain size distribution (sieved and laser diffraction data)). White triangles mark samples analysed texturally and black diamonds mark samples analysed geochemically (XRF and/or EPMA).

Figure 2

Component analysis and optical/secondary-electron SEM images. **a** Quantitative componentry of a 1997 sample (KRA-233) and the December 2018 samples (U23-2 and U10) using the 500 μm-1 mm size fraction, with the samples listed in chronological order. **b** KRA-233 deposit, showing mostly black juvenile clasts. **c** U10-2 tsunami deposit, dominated by 1883 Krakatau pumice clasts. **d** U23-2 ash deposit. Note the very high grain angularity and glassy nature of the grains. **e** U10-3B deposit, displaying more sub-angular grain morphologies and altered grains. **f** Secondary-electron (SE) SEM images of U23-2 ash grains with brittle or ductile fragmentation features. Left image displays a Pele's hair and a moss-like grain. Right image highlights a glass spherule. **g** SE SEM images of U10-6 ash grains with brittle or ductile fragmentation features. Left image shows a grain with stepped fractures. Right image displays a grain with a molten surface.

Figure 3

Graphs showing shape analysis of ash particles from U23-2 (**a**), U10-3B (**b**) and U10-4 (**c**) at three different grain size fractions (63-125 μm, 125-180 μm & 180-250 μm). Concavity index (CI) is plotted against axial ratio, with dashed line (CI=0.4) marking the threshold between dense and bubbly grains, after Liu et al. (2015a).

Binary images of examples of dense and bubbly grains (vesicular and glass shards) from each deposit are labelled on each diagram.

Figure 4

Backscattered-electron (BSE) SEM images of vesicular scoria with plagioclase feldspar microlite textures**. a** Tabular microlites in KRA-233. **b** Tabular and swallow-tail microlites in U23-2. **c** Tabular and acicular microlites in U10-3B. **d** Tabular, hopper and acicular microlites in U10-4. **e** Acicular microlites with prominent Fe-Ti rich compositional boundary layers in U10-6**. f** Acicular, tabular, hopper and swallow-tail microlites in U10-10.

Figure 5

EPMA chemical compositions of plagioclase, olivine, and pyroxene shown for KRA-233, U23-2 and U10. **a** Anorthite contents in microlites, microphenocrysts and phenocrysts of plagioclase. **b** Forsterite contents in microlites, microphenocrysts and phenocrysts of olivine. **c** and **d** Mg# for orthopyroxene (**c**) and clinopyroxene (**d**) in microlites, microphenocrysts and phenocrysts. Kernel density estimates are plotted on top of each diagram illustrating main distributions across all samples (and distinguishing KRA-233 from the 2018 samples in plagioclase).

Figure 6

Temporal variations of N_A (**a**), crystallinity (**b**), mean microlite size (**c**), aspect ratio (**d**) and mean ascent rate (**e**) (grey bars represent ascent rate ranges using range of water content values estimated from plagioclase-melt hygrometry of Putirka (2008)) for plagioclase feldspar microlites in vesicular microlite-rich scoriae from KRA-233 (1997) and December 2018 samples (U23-2 and U10).

Figure 7

Conceptual model for syn- and post-collapse volcanic processes at Anak Krakatau from 22 Dec. 2018 to early Jan. 2019. **a** Pre-collapse: open, steady-state conditions, typical of the Strombolian feeder system reflected in low ascent velocities and microlite textures of KRA-233 and U23-2. P_{c1} represents an average pre-collapse conduit pressure. **b** Phase A: Lateral collapse and unloading causing downward propagating decompression and an intense explosion from unloading of the surficial conduit; limited seawater interaction, and deposition of U23-2. **c** Phase B: Destabilisation, decompression and deeper tapping of the conduit facilitating fast ascent of U10-3 (Surtseyan vent widening) and U10-4 (sustained Surtseyan activity). $P_{c2} < P_{c1}$ represents Phase B with conditions of a highly depressurised conduit (P_{c2}) relative to pre-collapse conduit pressure (P_{c1}). **d** Phase C: System gradually re-stabilised with ascent characterised by lower velocities and decompression rates (U10-6 to U10-10). $P_{c3} > P_{c2}$ represents Phase C conduit pressure re-stabilising following Phase B eruptions and partial edifice regrowth.

Table captions

Table 1

Textural characteristics of plagioclase microlites in vesicular microlite-rich scoriae from Anak Krakatau, with estimated ascent rates (KRA-233: 1997 Strombolian sample; U23-2 and U10- : 2018 samples; n denotes the number of crystals analysed).

Supplementary Material

Supplementary Table 1. Sample list with location and analyses.

Supplementary Table 2. Summary of clast component types (evaluated on 500 μm to 1 mm sieved size fraction).

Supplementary Table 3. Compositional analyses (XRF & EPMA) for Anak Krakatau 2018 and 1997 tephra samples.

Supplementary Table 4. Temperatures and pressures calculated using thermobarometers of plagioclase and orthopyroxene (Putirka, 2008).

Appendix 1. Analytical methods.

Supplementary Figures (S.1 to S.5)

S.1 Sentinel 2 L1C satellite images of the Krakatau archipelago in infrared based on bands 8, 4 & 3. Dense vegetation is highlighted in red and tephra deposition is shown in dark grey. **a** Pre-collapse image showing extensive fresh ash deposition/lava emplacement on Anak Krakatau and potential minor deposition on Panjang taken on 16 Nov. 2018. **b** Post-collapse image of significant ash deposition and vegetation loss on Anak Krakatau and Panjang (image taken on 10 Jan. 2019). White arrow highlights plume of reddish-orange (infrared = turquoise) water emanating from uncovered hydrothermal system off the SW island coastline.

S.2 **a** Dec. 2018 stratigraphies on Panjang (P) and Sertung (S). Black background shading indicates the only well-correlated layer (U10-3 and NP2-1) throughout the sections based on lithological characteristics (i.e., 0.5 cm-thick layer of purple indurated ash; see right-hand side image in **b**). Colours and grain-size are based on field descriptions. White triangles mark samples analysed texturally and black diamonds mark samples analysed geochemically (XRF and/or EPMA). **b** Left image: close-up of U10 sequence. Right image: close-up of layer U10-3 showing the yellow oxidised crust at the surface of a purple indurated ash immediately overlying the pumiceous tsunami deposit (U10-2). **c** Tsunami simulation at ~380s displaying maximum envelope for tsunami wave inundation at site U10 (~7 m wave height). Simulation used the 2D FUNWAVE model at 50 m resolution (Grilli et al. 2019).

S.3 Major element compositions of matrix glasses (**a, b, c, d,** and **e**). **f** Whole-rock total alkali vs. silica (TAS) diagram of 2018 products (U23-2, U10, NP1), plotted alongside previously published data of other recent eruptive products (^Walter et al. 2019; *includes data from Gardner et al. 2013).

S.4 Examples of manually outlined plagioclase feldspar microlites (black) used for the 2D textural analysis.

S.5 Batch microlite textural parameters for KRA-233, U23-2 and U10 samples. **a** Areal feldspar microlite number density (NA mm^{-2}) vs. groundmass feldspar microlite crystallinity (φ). **b** Areal feldspar microlite number density vs. mean microlite size (Sn, μm). **c** Areal feldspar microlite number density vs. aspect ratio.

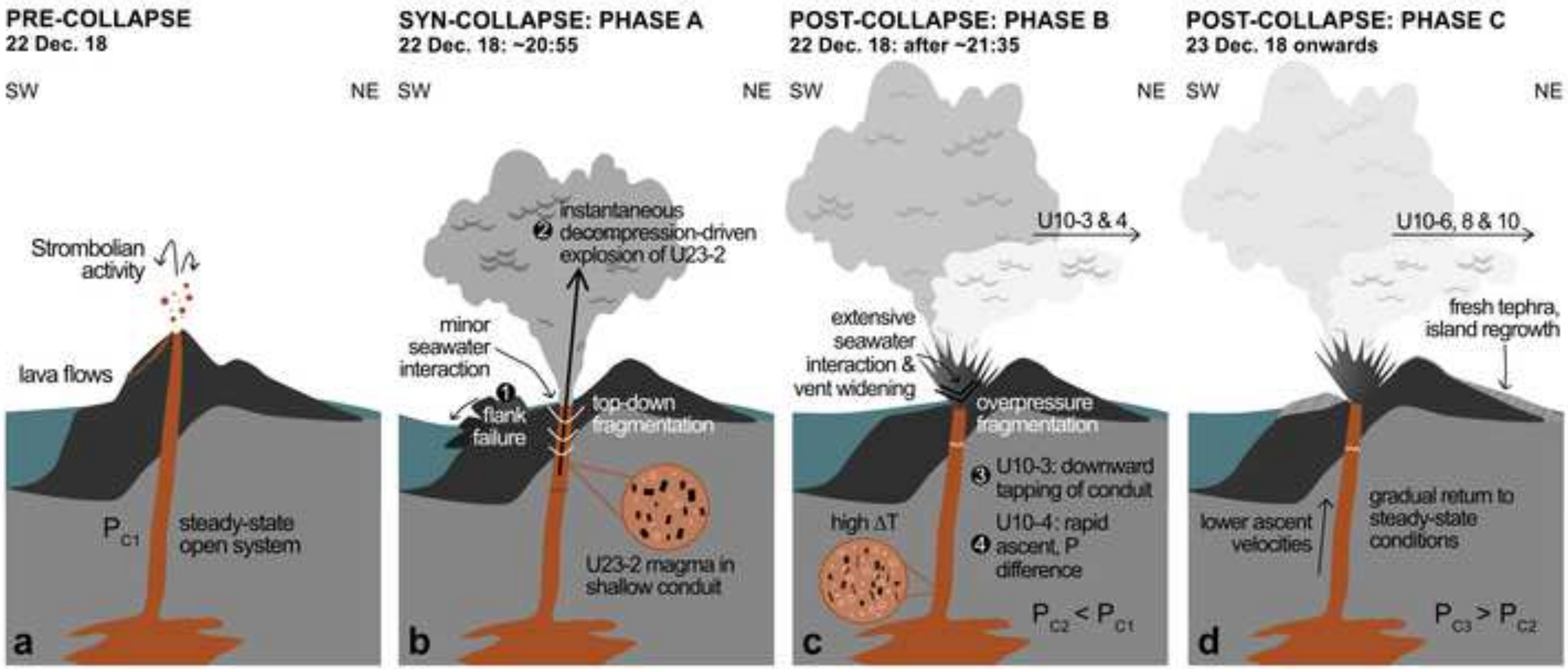

P_C = relative conduit pressure
ΔT = undercooling
NOT TO SCALE

Figure

Click here to access/download;Figure;FIG1_FINAL.tiff

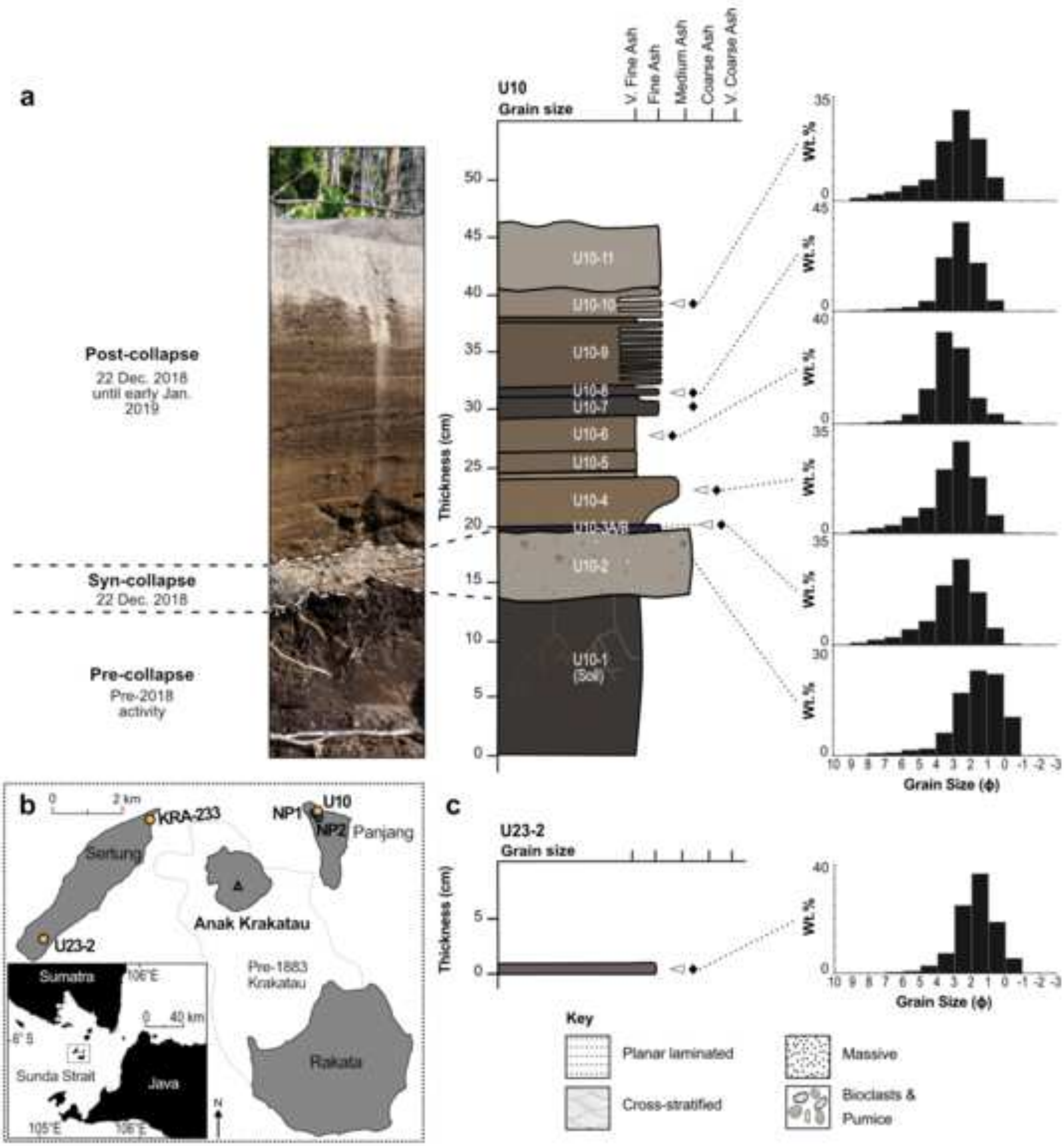

Figure

Click here to access/download;Figure;FIG2_FINAL.tiff

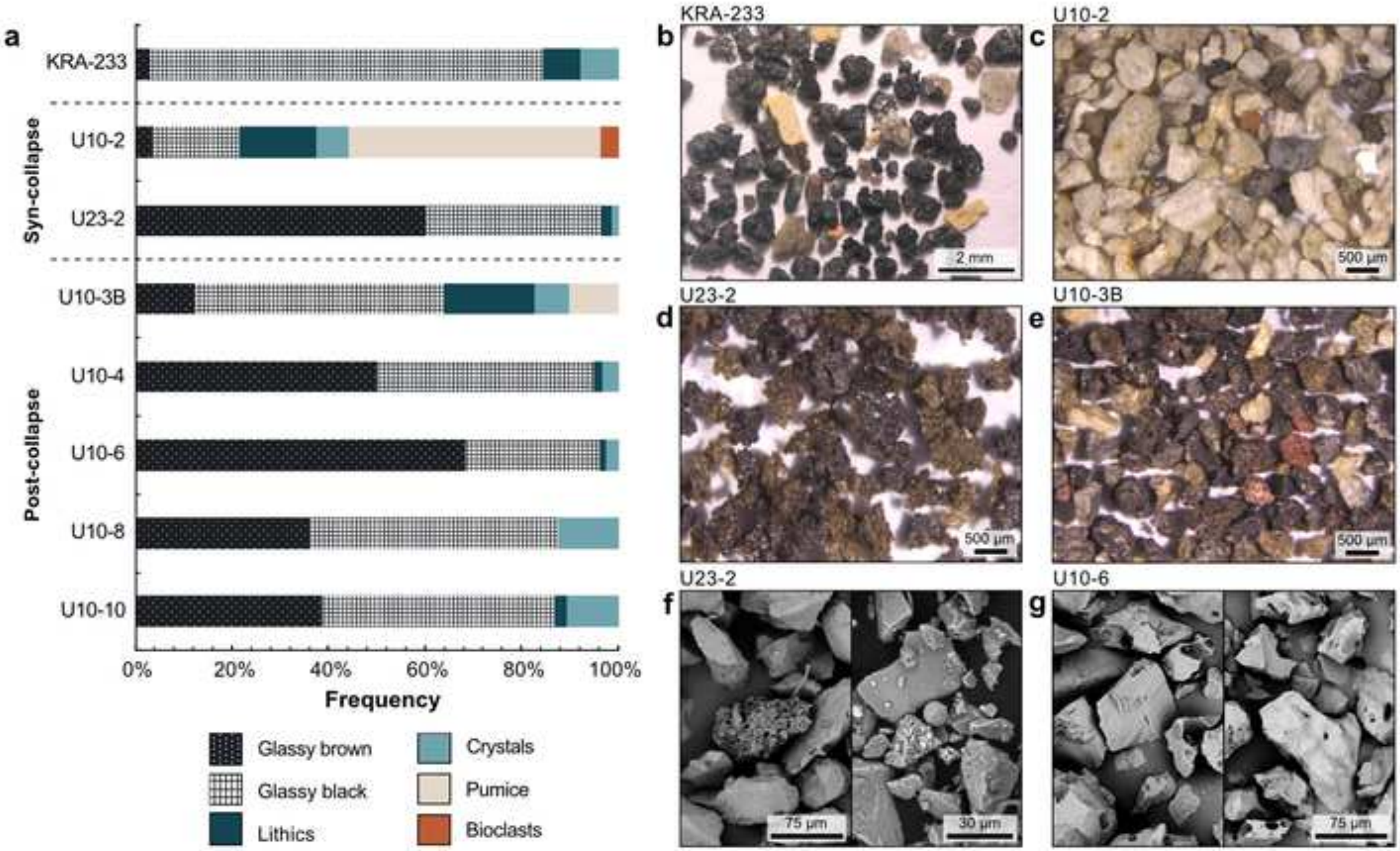

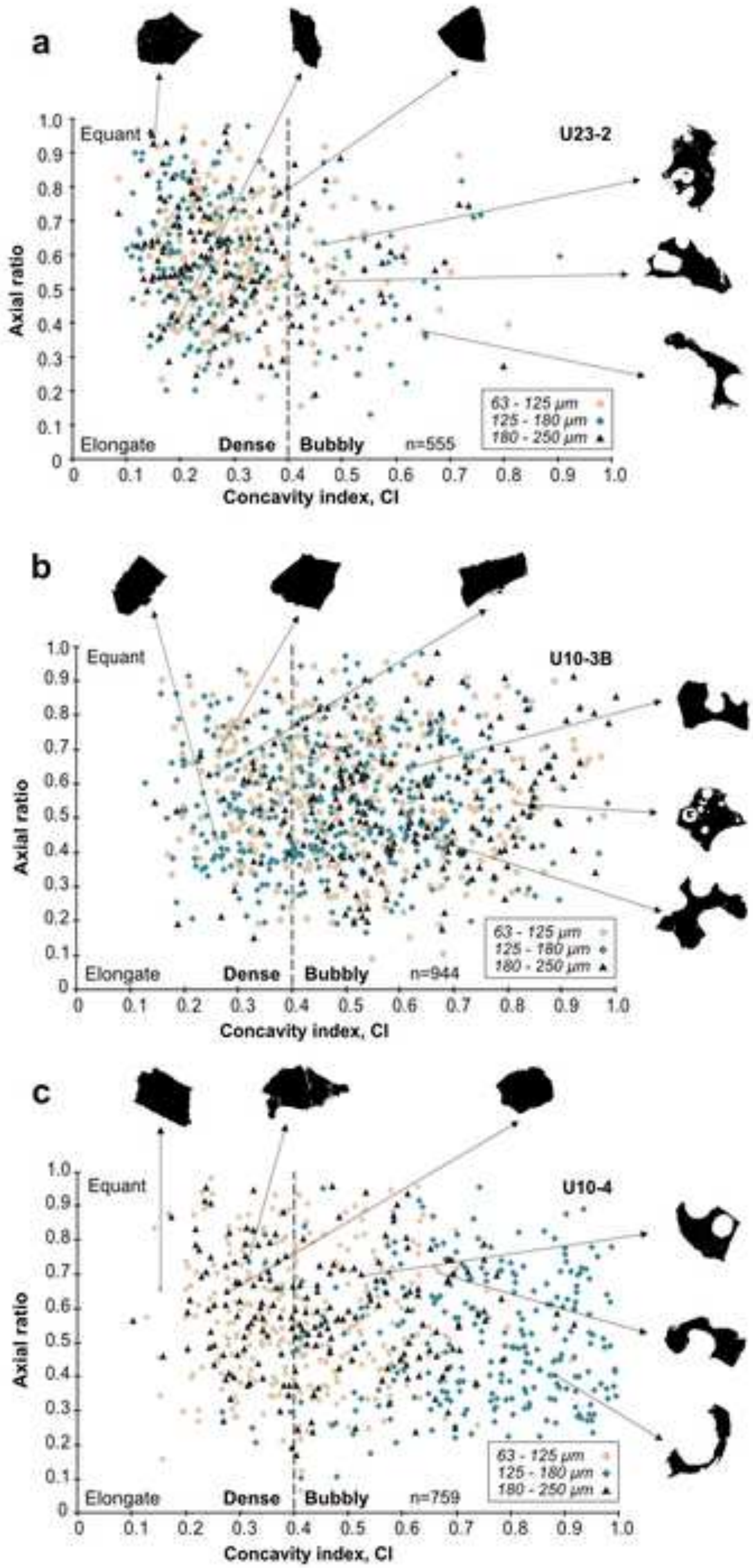
a
U23-2
Equant
Elongate
Dense
Bubbly
n=555
63 - 125 μm
125 - 180 μm
180 - 250 μm
Axial ratio
Concavity index, CI
b
U10-3B
Equant
Elongate
Dense
Bubbly
n=944
63 - 125 μm
125 - 180 μm
180 - 250 μm
Axial ratio
Concavity index, CI
c
U10-4
Equant
Elongate
Dense
Bubbly
n=759
63 - 125 μm
125 - 180 μm
180 - 250 μm
Axial ratio
Concavity index, CI

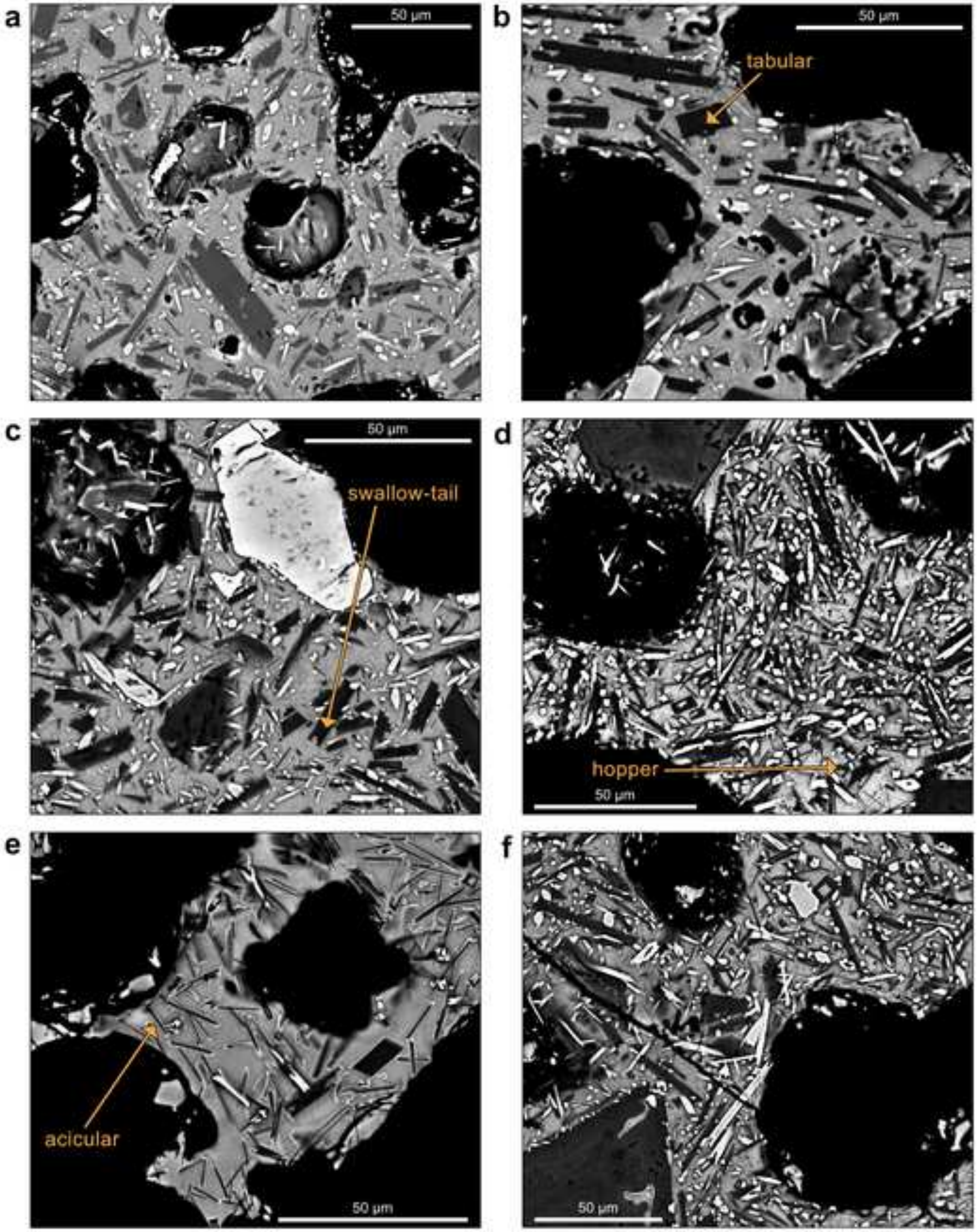
a
50 µm
b
50 µm
tabular
c
50 µm
swallow-tail
d
hopper
50 µm
e
acicular
50 µm
f
50 µm

Figure

Click here to access/download;Figure;FIG5_FINAL.tiff

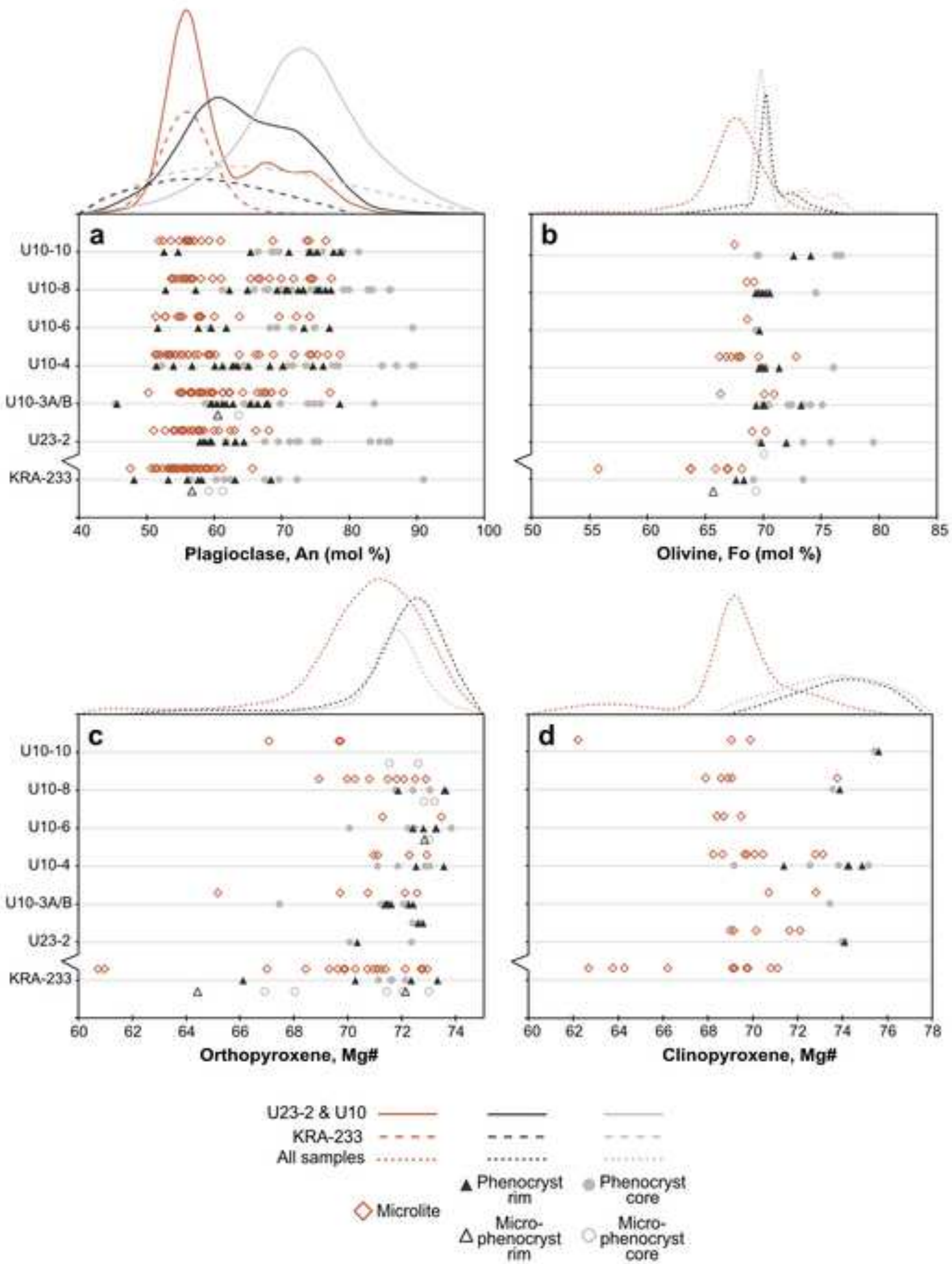

Figure

Click here to access/download;Figure;FIG6_FINAL.tiff

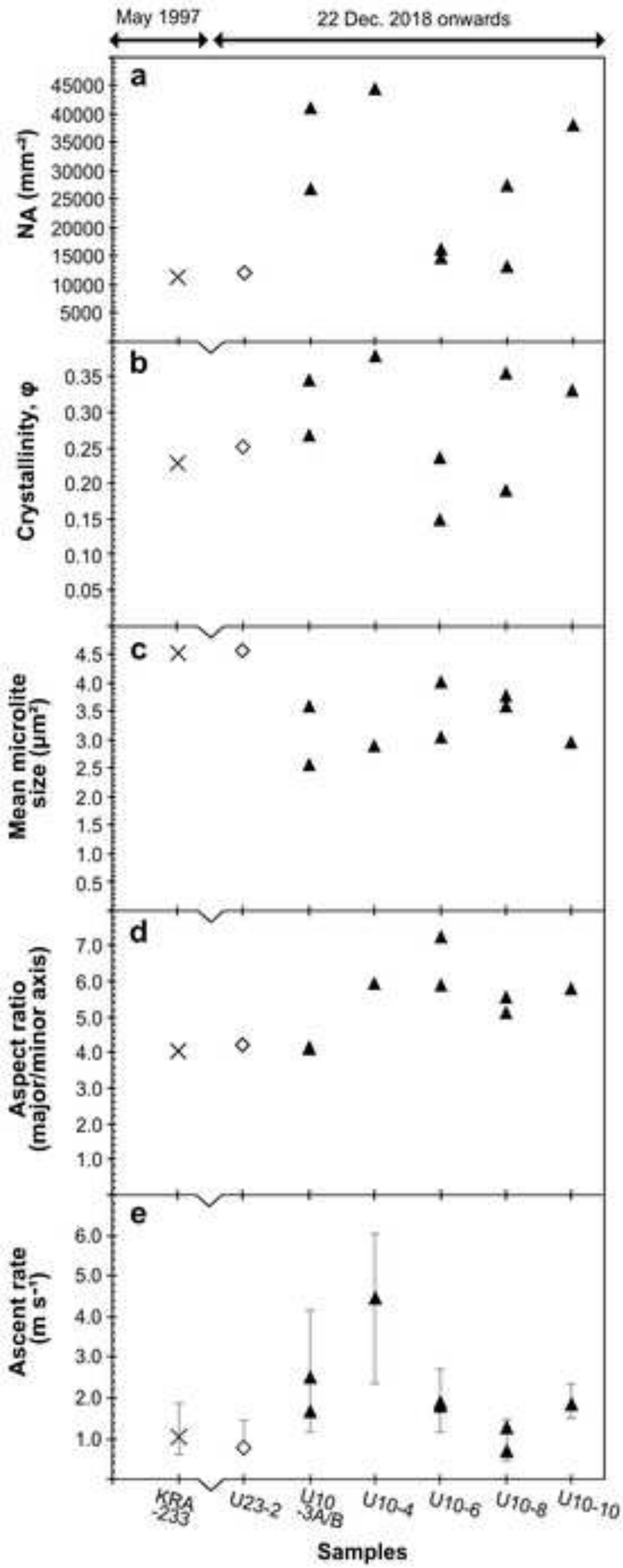

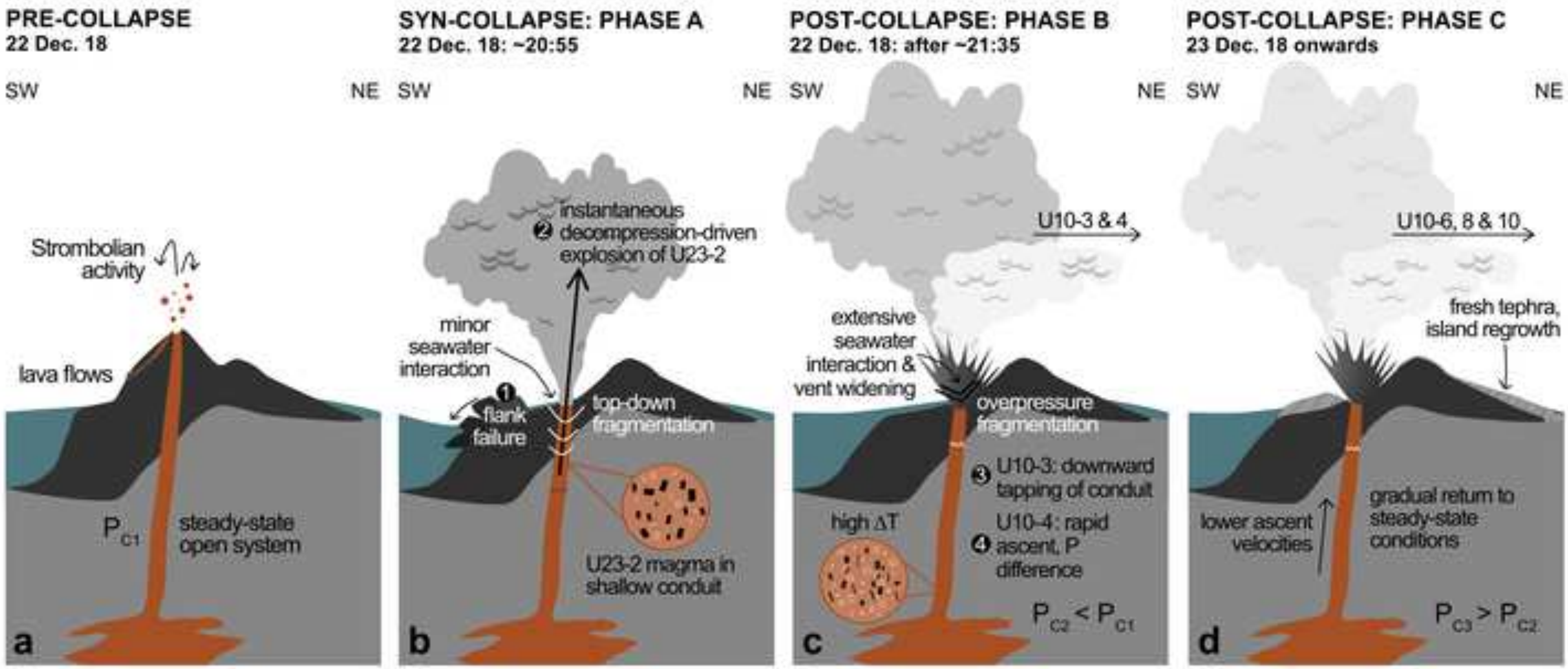
PRE-COLLAPSE
22 Dec. 18
SW
NE
Strombolian activity
lava flows
P C1
steady-state open system
a
SYN-COLLAPSE: PHASE A
22 Dec. 18: ~20:55
SW
NE
2 instantaneous decompression-driven explosion of U23-2
minor seawater interaction
1 flank failure
top-down fragmentation
U23-2 magma in shallow conduit
b
POST-COLLAPSE: PHASE B
22 Dec. 18: after ~21:35
SW
NE
U10-3 & 4
extensive seawater interaction & vent widening
overpressure fragmentation
3 U10-3: downward tapping of conduit
4 U10-4: rapid ascent, P difference
high ΔT
P C2 < P C1
c
POST-COLLAPSE: PHASE C
23 Dec. 18 onwards
SW
NE
U10-6, 8 & 10
fresh tephra, island regrowth
lower ascent velocities
gradual return to steady-state conditions
P C3 > P C2
d

Click here to access/download
Figure (high-resolution)
FIG4_FINAL_highres.tiff

Figure (high-resolution)

Click here to access/download
Figure (high-resolution)
FIG7_FINAL_highres.tiff

Sample	2D areal measurements							3D volumetric measurements	
	n	Image area (μm^2)	N_A (mm^{-2})	Plag. area %	Plag. area fraction, φ	Mean crystal size, S_n (μm^2)	Aspect ratio (major/minor axis)	N_V (mm^{-3})	Mean ascent rate (m s^{-1})
KRA-233	403	35561	11194	16.28	0.23	4.54	4.08	2466412	1.04
U23-2	784	65328	12062	14.59	0.25	4.56	4.19	2644251	0.76
U10-3A	914	33612	26882	24.10	0.35	3.58	4.14	7501290	1.69
U10-3B	1110	27164	41111	22.93	0.27	2.56	4.09	16074394	2.49
U10-4	980	22475	44545	23.40	0.38	2.92	5.93	15278638	4.45
U10-6_1	716	43873	16273	10.43	0.15	3.04	7.28	5349256	1.88
U10-6_2	774	53431	14604	13.56	0.24	4.03	5.91	3619626	1.81
U10-8_1	577	21186	27476	25.63	0.36	3.60	5.14	7631114	1.26
U10-8_2	507	37593	13342	16.17	0.19	3.78	5.55	3527747	0.71
U10-10	1215	32271	37969	21.56	0.33	2.96	5.79	12843341	1.83

Declaration of interests

☒ The authors declare that they have no known competing financial interests or personal relationships that could have appeared to influence the work reported in this paper.

☐The authors declare the following financial interests/personal relationships which may be considered as potential competing interests:

CRediT authorship contribution statement

KSC led the analysis, and with SFLW developed the approach and methodology, interpretation and writing, with contributions from MC, ALMN and SLE. All authors contributed to the final interpretation and text. Initial project development was led by SFLW, MC, SLE, with input throughout the data collection and analysis stage from ALMN, MA, MEMN, DRT, SNC, AN, JH, SD, CH, IAK and NK.